

It's a Trap! Aldolase-Prescribed C₄ Deoxyradiofluorination Affords Intracellular Trapping and the Tracing of Fructose Metabolism by PET

Alexia Kirby^{1,2}, Dominic Graf^{2,3}, Mojmír Suchý^{2,3}, Nicholas D. Calvert^{2,3}, Thomas A. Charlton², Robert N. Ben², Christina L. Addison⁴⁻⁶, and Adam Shuhendler^{1,2,3,7}

¹Department of Biology, University of Ottawa, Ottawa, Ontario, Canada; ²Heart Institute, University of Ottawa, Ottawa, Ontario, Canada; ³Department of Chemistry and Biomolecular Sciences, University of Ottawa, Ottawa, Ontario, Canada; ⁴Program for Cancer Therapeutics, Ottawa Hospital Research Institute, Ottawa, Ontario, Canada; ⁵Department of Medicine, University of Ottawa, Ottawa, Ontario, Canada; ⁶Department of Biochemistry, Microbiology, and Immunology, University of Ottawa, Ottawa, Ontario, Canada; and ⁷Brain and Mind Research Institute, University of Ottawa, Ottawa, Ontario, Canada

Fructose metabolism has been implicated in various diseases, including metabolic disorders, neurodegenerative disorders, cardiac disorders, and cancer. However, the limited availability of a quantitative imaging radiotracer has hindered its exploration in pathology and diagnostic imaging. **Methods:** We adopted a molecular design strategy based on the catalytic mechanism of aldolase, a key enzyme in fructolysis. We successfully synthesized a radiodeoxyfluorinated fructose analog, [¹⁸F]4-fluoro-4-deoxyfructose ([¹⁸F]4-FDF), in high molar activity. **Results:** Through heavy isotope tracing by mass spectrometry, we demonstrated that C₄-deoxyfluorination of fructose led to effective trapping as fluorodeoxysorbitol and fluorodeoxyfructose-1-phosphate in vitro, unlike C₁- and C₆-fluorinated analogs that resulted in fluorolactate accumulation. This observation was consistent in vivo, where [¹⁸F]6-fluoro-6-deoxyfructose displayed substantial bone uptake due to metabolic processing whereas [¹⁸F]4-FDF did not. Importantly, [¹⁸F]4-FDF exhibited low uptake in healthy brain and heart tissues, known for their high glycolytic activity and background levels of [¹⁸F]FDG uptake. [¹⁸F]4-FDF PET/CT allowed for sensitive mapping of neuro- and cardioinflammatory responses to systemic lipopolysaccharide administration. **Conclusion:** Our study highlights the significance of aldolase-guided C₄ radiodeoxyfluorination of fructose in enabling effective radiotracer trapping, overcoming limitations of C₁ and C₆ radioanalogs toward a clinically viable tool for imaging fructolysis in highly glycolytic tissues.

Key Words: molecular imaging; fructose; inflammation; metabolic tracing; PET; radiofluorination

J Nucl Med 2024; 65:475–480
DOI: 10.2967/jnumed.123.266905

The use of fructose as an energy source (i.e., fructolysis) during the onset and progression of a variety of diseases is a continued area of both fundamental and clinical investigation, with inflammation-induced energy crises activating a fructolytic state in the affected tissues. In the heart, the switch from glycolysis to

fructolysis has been identified in cardiac hypertrophy (1,2) and myocardial infarction (3), with data supporting a hypoxia-driven activation of this aberrant metabolic program. In the brain, fructolysis is thought to be a putative driver of Alzheimer disease (4) and has been shown to be proinflammatory, with negative implications after traumatic or stroke injury and in psychologic health (5). The switch from glucose to fructose as an energy source may also be a key oncologic driver, promoting the progression of a variety of solid tumors through the concerted transcriptional activation of transport and metabolic machinery (6–10). Excessive fructose consumption has also been associated with a liver-centered metabolic syndrome thought to drive obesity and diabetes (11) and to be a major player in the related cardiovascular (11,12), ocular (13), and degenerative (12) outcomes. The fundamental importance of fructolysis in a range of diseases has encouraged the development of methods to noninvasively map fructose metabolism, a challenge that is currently an unsolved problem.

Canonic fructose metabolism begins with glucose transporter 5-mediated transport into the cell and ketohexokinase-mediated trapping of the sugar as fructose-1-phosphate (Fig. 1A) (11). Phosphorylation is followed by carbon chain scission through the activity of aldolase enzymes and the subsequent formation of glyceraldehyde-3-phosphate, which continues to be metabolized downstream. This metabolic cascade has been followed using noninvasive in vivo imaging in preclinical models, taking advantage of the spectroscopic capabilities of deuterium and hyperpolarized MRI (14,15). Toward the clinical translational use of fructolysis as a quantitative imaging biomarker, previous work has attempted to trace fructose metabolism by PET by installing radiofluorine (¹⁸F) at the C₁ or C₆ positions (16–20). The early metabolic trapping of fructose would lend itself to tracing of aberrant metabolism similarly to [¹⁸F]FDG, the most extensively applied PET nuclear diagnostic used in the clinic. However, the significant bone-derived radioactivity observed by PET from previous radiodeoxyfluorofructose analogs suggests that cellular trapping was not achieved (Fig. 1A).

To produce a radiofluorinated fructose analog that is trapped in cells as its phosphorylated metabolite, we closely examined the catalytic mechanism of aldolase, the enzyme for which fructose-1-phosphate is a substrate (Fig. 1B) (21). Within the aldolase active site, the initial Schiff base formation with the C₂-carbonyl is immediately followed by a base-mediated proton abstraction from the C₄-hydroxyl moiety to induce C–C bond scission. Given the critical role of the C₄-OH in the catalytic mechanism, we hypothesized that the

Received Oct. 19, 2023; revision accepted Dec. 6, 2023.
For correspondence or reprints, contact Adam Shuhendler (adam.shuhendler@uottawa.ca).
Published online Jan. 25, 2024.
COPYRIGHT © 2024 by the Society of Nuclear Medicine and Molecular Imaging.

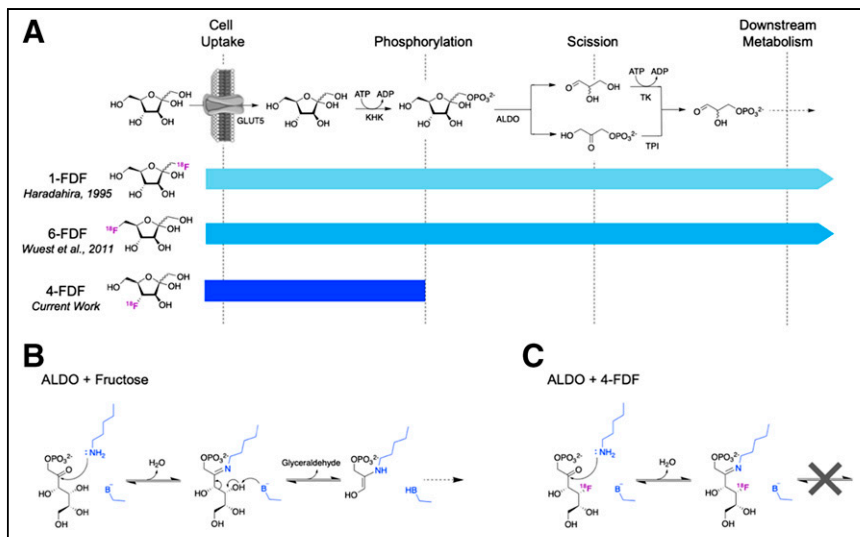


FIGURE 1. Fructose metabolism tracing, then and now. (A) Initial metabolism of fructose comprises cell uptake, phosphorylation, and scission steps mediated by glucose transporter 5, ketohexokinase, and aldolase, respectively. Proposed progression of existing fructose-derived radiotracers, 1-FDF and 6-FDF, as well as hypothesized trapping of proposed 4-FDF, are shown. (B) First 2 steps of aldolase-mediated scission of fructose. (C) Proposed effect of C_4 deoxyfluorination on aldolase mechanism. ADP = adenosine diphosphate; ALDO = aldolase; ATP = adenosine triphosphate; B^- = basic residue; blue = aldolase active site residue; GLUT = glucose transporter; KHK = ketohexokinase; TK = triose kinase; TPI = triosephosphate isomerase.

deoxyfluorination of the C_4 position would prevent aldolase-mediated scission (Fig. 1C), resulting in the trapping of 4-fluoro-4-deoxyfructose (4-FDF) within the metabolic cell of origin (Fig. 1A). In the current work, we generated 4-FDF, evaluated its metabolic flux in vitro relative to 1-fluoro-1-deoxyfructose (1-FDF) and 6-fluoro-6-deoxyfructose (6-FDF), and compared the PET imaging of [^{18}F]4-FDF with that of [^{18}F]6-FDF and [^{18}F]FDG in tracing metabolism in mouse models of cancer and systemic inflammation.

MATERIALS AND METHODS

Synthesis

All synthetic procedures are described in detail in the supplemental materials (available at <http://jnm.snmjournals.org>).

In Vitro Metabolic Tracing

All procedures for metabolic tracing of [$U^{13}C$]–fructose analogs are provided in the supplemental materials.

Animal Models

All animal research was approved by the institutional animal care and use committee of the University of Ottawa under animal use protocols SCE-3254-R3 (tumor study) and SCE-4019-A1 (inflammation study). Mice were housed in standard cages, kept on a 12-h light–dark cycle, and provided standard rodent chow and water ad libitum.

Eight-week-old female nu/nu mice were inoculated, subcutaneously under the left shoulder, with 10×10^6 HepG2 cells suspended in 50% Matrigel (Corning)–50% Dulbecco modified Eagle medium. Within 3 wk of implantation, the mice were imaged by PET/CT.

Eight-week-old male C57BL/6 mice received a 5 mg/kg dose of lipopolysaccharide through intraperitoneal injection 24 h before planned PET/CT imaging. For 12 h after receiving the injection, they were kept warm, given fluids subcutaneously, monitored, and scored for severity of response to lipopolysaccharide as published previously (22).

PET/CT Imaging

PET/CT imaging was performed on an Si78PET/CT scanner with a 4-position hotel having adjustable isoflurane and respiratory monitoring for each position (Bruker USA). Tail veins were catheterized, and an anatomic CT scan was acquired over the whole of the mouse bodies using the rat settings. The PET acquisition was started just before a bolus intravenous injection of approximately 7.4 MBq of radiotracer. Dynamic scans were acquired in list mode over 45 min and sorted into sixteen 0.5-mm sinogram bins for image reconstruction (4×15 s, 4×60 s, and 8×300 s). Iterative reconstruction was performed using 3-dimensional ordered-subsets expectation maximization followed by fast maximum a posteriori estimation using Paravision 360 software, version 3.4 (Bruker). Four-mouse images were split into individual mice, and the bed was removed using PMOD (Bruker). VivoQuant, version 2022 (InviCRO), was used to visualize tissue uptake, for definition of 3-dimensional volumes of interest, and to visualize in 3 dimensions for volume rendering. The count densities were averaged for all volumes of interest at each time point to obtain a time–activity curve. Tumor and tissue time–activity curves

were normalized to injected dose, measured by a CRC-15 PET dose calibrator (Capintec, Inc.), and expressed as percentage injected dose per cubic centimeter of tissue.

Statistical Analyses

Statistical analyses were performed using Prism (version 9.5.0; GraphPad, Inc.). Comparisons across more than 2 groups were performed by 1-way ANOVA followed by the Tukey test for honestly significant differences. Normality was assumed when appropriate for all datasets. Before ANOVA, the Levene test was used to confirm equal variance, and visual quantile–quantile plot analysis was used to confirm homoscedasticity.

RESULTS

To characterize the structure–activity effect of fructose deoxyfluorination on metabolic flux, we evaluated the metabolism of isotopically labeled [$U^{13}C$]–fructose and of [$U^{13}C$]–1-FDF, [$U^{13}C$]–6-FDF, and [$U^{13}C$]–4-FDF deoxyfluorinated fructose analogs in vitro in HepG2 human hepatocarcinoma cells by mass spectrometry (Fig. 2). HepG2 was chosen as a model cell line because of a recent report by Tee et al. outlining its propensity for fructolysis (23). [$U^{13}C$]–1-FDF and [$U^{13}C$]–6-FDF were synthesized according to previously published methods (16,17), and [$U^{13}C$]–4-FDF was synthesized as described in the supplemental materials. After confirming that [$U^{13}C$]–fructose was metabolized as expected through both fructolytic and polyol pathways to establish a baseline for tracing fructose metabolism (Fig. 2A), we next examined the relative flux of the deoxyfluorinated analogs (Fig. 2B). [$U^{13}C$]–1-FDF showed limited metabolism through the polyol pathway, with most of the ^{13}C –labeled cellular product being [$U^{13}C$]–deoxyfluorolactate (Fig. 2B). Of critical importance, however, is that although [$U^{13}C$]–6-FDF metabolism produced a substantial amount of [$U^{13}C$]–deoxyfluorolactate through scission and downstream metabolism (Fig. 2B), [$U^{13}C$]–4-FDF metabolism halted at [$U^{13}C$]–4-fluoro-deoxy-1-phosphate, the fructolytic metabolite that

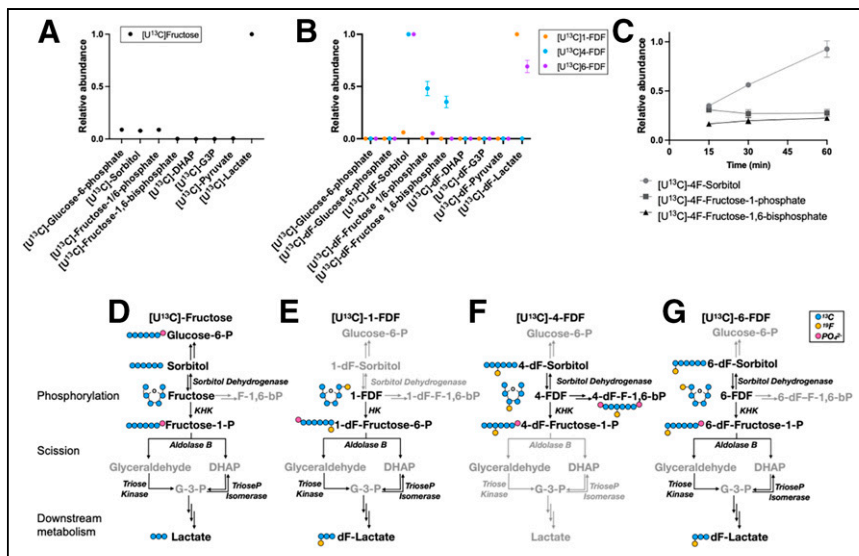


FIGURE 2. Decoding positional effects of fructose deoxyfluorination on its metabolism in vitro in HepG2 cells by mass spectrometry. (A and B) Relative abundance of metabolites from isotopically labeled [^{13}C]-fructose (A) and [^{13}C]-1-FDF, [^{13}C]-4-FDF, and [^{13}C]-6-FDF (B). (C) Time course of metabolite generation from [^{13}C]-4-FDF. (D–G) Metabolism schemes based on mass spectrometry results for [^{13}C]-fructose (D), [^{13}C]-1-FDF (E), [^{13}C]-4-FDF (F), and [^{13}C]-6-FDF (G). Black text = detected metabolite or pathway; blue circle = ^{13}C ; dF = deoxyfructose; DHAP = dihydroxyacetone phosphate; G3P = glyceraldehyde-3-phosphate; gray text = undetected metabolite or pathway; HK = hexokinase; KHK = ketohexokinase; pink circle = PO_4^{2-} ; yellow circle = ^{19}F .

is the substrate for aldolase-mediated scission (Fig. 2B). Uniquely, [^{13}C]-4-FDF metabolism also resulted in the accumulation of [^{13}C]-4-fluorodeoxyfructose-1,6-bisphosphate. A key outcome of this experiment was the confirmation that all deoxyfluorinated analogs of fructose entered the cells rapidly (within 30 min). To validate the observed metabolite trapping, a time course evaluation of [^{13}C]-4-FDF metabolism was performed over 60 min, demonstrating the steady-state accumulation of [^{13}C]-4-fluorodeoxyfructose-1-phosphate and [^{13}C]-4-fluorodeoxyfructose-1,6-bisphosphate and the increase in [^{13}C]-4-fluorodeoxysorbitol throughout the 60 min of incubation (Fig. 2C). The results of this study support our hypothesis that, like native fructose (Fig. 2D), neither [^{13}C]-1-FDF (Fig. 2E) nor [^{13}C]-6-FDF is metabolically trapped (Fig. 2G) but that the deoxyfluorination of fructose at C_4 prevents aldolase-mediated hexose scission and traps the deoxyfluorinated fructose analog in the cell (Fig. 2F). By rethinking the site of deoxyfluorination to afford metabolic trapping as informed by the catalytic mechanism of the enzyme immediately ensuing to the intended trapped metabolite, we uncovered the chemical requirements for mapping fructolysis.

To proceed toward fructolysis mapping in vivo by PET, a radio-deoxyfluorination approach was designed to afford nucleophilic substitution at the C_4 position using standard radiochemical techniques somewhat related to the routine production of [^{18}F]FDG. Details of the synthesis of compounds 1–4 have been reported previously (24), and further synthetic steps and chemical characterization for compounds 5, 6, and [^{18}F]4-FDF are provided in the supplemental materials (Supplemental Schemes 1–5; Supplemental Figs. 3–232). The precursor synthesis began with C_1 -OH methylation and dimethyl ketalation of C_2 -OH and C_3 -OH, followed by the protection of C_6 -OH with chloromethyl methyl ether in order to isolate the C_4 -OH (Fig. 3A). The stereochemistry at C_4 was then inverted in 2 steps and was converted to the tosylated precursor 5 (Fig. 3A). The C_4 stereoinversion was necessary to allow the subsequent

radio-deoxyfluorination step to restore the C_4 -D-enantiomer after the [^{18}F]tetraethylammonium fluoride-mediated nucleophilic attack (Fig. 3B, 6). Rapid on-module deprotection resulted in [^{18}F]4-FDF in good radiochemical yield (25%–30%) and molar activity (25.3 ± 0.6 GBq/nmol) comparable to that resulting from the routine production of [^{18}F]FDG (25).

With the confirmation of cell uptake and intracellular trapping of [^{13}C]-4-FDF, and the successful production of the radiofluorinated analog, the biodistribution of [^{18}F]4-FDF was evaluated in a heterotopic HepG2 xenograft mouse model and compared with the biodistribution of [^{18}F]6-FDF and [^{18}F]FDG (Fig. 4). [^{18}F]1-FDF was not evaluated in vivo since it was already demonstrated to be poorly retained in cells in vitro and in vivo (18). After intravenous injection, [^{18}F]4-FDF was found to accumulate in the tumor, with renal exceeding hepatobiliary excretion (Fig. 4A). This pattern of radiotracer retention was similarly observed for [^{18}F]6-FDF, with a key difference, however, being bone uptake (Fig. 4B). Although any bone uptake was limited to less than 2% injected dose/mL for [^{18}F]4-FDF (Fig. 4A;

Supplemental Fig. 2), bone uptake was 3.69-fold higher (>7% injected dose/mL) after [^{18}F]6-FDF imaging (Fig. 4B and 4D). This extensive bone uptake, which continues to increase over time (Supplemental Fig. 2), was reported previously for [^{18}F]6-FDF (17) and is supported by the metabolic flux outcomes of [^{13}C]-6-FDF demonstrating the production of [^{13}C]fluorodeoxylactate (Figs. 2B and 2G).

Overall, the accumulation of [^{18}F]4-FDF in normal mouse tissues was lower than that of [^{18}F]FDG (Figs. 4A vs. 4C). Notably, the area under the time-activity curve in the brain and heart was 6.01- and 5.29-fold greater, respectively, for [^{18}F]FDG than for [^{18}F]4-FDF (Fig. 4D), suggesting that healthy brain and heart have a limited dependence on fructolysis for energy production. To further investigate whether a fructolytic switch occurs in inflammatory neural and cardiac tissues, as previously proposed (1–5,12), a mouse model of systemic inflammation was examined (Fig. 5). Mice receiving saline vehicle (Fig. 5A) or intraperitoneal bacterial cell wall lipopolysaccharide, as previously described (Fig. 5B) (22), were imaged by [^{18}F]4-FDF PET/CT 24 h after injection. A significant increase in cardiac (Figs. 5D and 5F) and brain (Figs. 5C and 5E) uptake of [^{18}F]4-FDF was observed after lipopolysaccharide treatment in all mice evaluated. Both the brain and the heart demonstrated inflammatory responses to lipopolysaccharide stimulation within 24 h of its systemic introduction, mediated through toll-like receptor engagement on microglia or cardiac adrenergic cells (26,27). The low uptake of [^{18}F]4-FDF in healthy brain and heart contributed to an increased signal-to-noise ratio for the mapping of cardio- and neuroinflammation (Figs. 5C and 5D).

DISCUSSION

Although the pathologic switch to fructose metabolism has been implicated in a variety of metabolic, neurodegenerative, and cardiac diseases, as well as being a driver or consequence of

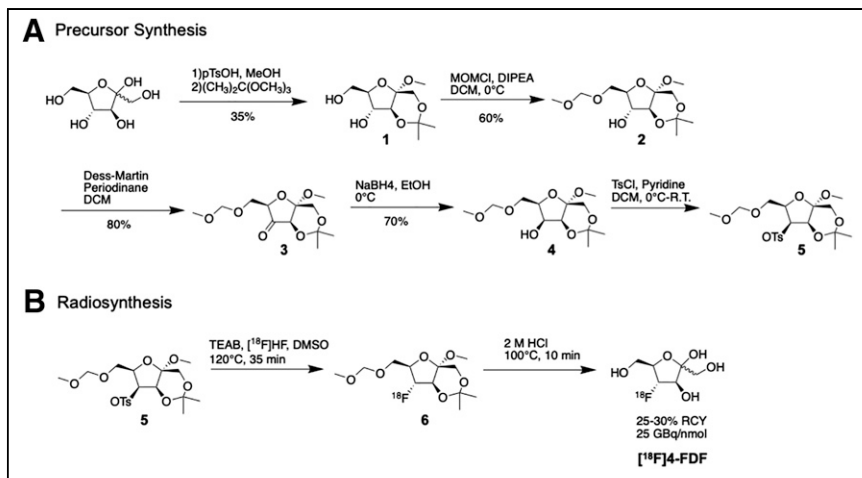


FIGURE 3. Syntheses of radiochemical precursor (A) and final radiofluorinated [^{18}F]4-FDF (B). pTsOH = *para*-toluenesulfonic acid; MeOH = methanol; MOMCl = chloromethyl methyl ether; DIPEA = *N,N*-diisopropylethylamine; DCM = dichloromethane; EtOH = ethanol; TsCl = *para*-toluenesulfonyl chloride; R.T. = room temperature; TEAB = tetraethylammonium bromide; DMSO = dimethylsulfoxide; RCY = radiochemical yield.

malignancy, the evaluation of fructolysis in fundamental mechanisms of pathology and its implementation as a diagnostic imaging biomarker has been limited by the lack of a quantitative tracer for imaging-based analysis. Taking a molecular design approach informed by the catalytic mechanism of aldolase, the fructolytic enzyme whose activity must be blocked in order to afford metabolic trapping, we synthesized a radiodeoxyfluorinated analog of fructose: [^{18}F]4-FDF. Radiosynthesis was realized on a standard radiofluorination module in good yield and molar activity, mimicking the nucleophilic radiofluorination and acid-catalyzed deprotection used for the preparation of [^{18}F]FDG (Fig. 3).

As compared with previously reported C_1 and C_6 radioanalogs of fructose, using heavy-isotope tracing by mass spectrometry we demonstrated that the C_4 deoxyfluorination of fructose led to trapping as fluorodeoxysorbitol and fluorodeoxyfructose-1-phosphate *in vitro* (Fig. 2). Key differences in polyol pathway flux were also observed between the different fluorinated positional isomers. The limited polyol flux observed for C_1 fluorodeoxyfructose is likely the result of improper substrate positioning in the sorbitol dehydrogenase active site by the deoxyfluorination of C_1 , which prevents a critical $\text{C}_1\text{-OH}$ -to-zinc interaction (28). In contrast, both [^{13}C]6-FDF and [^{13}C]4-FDF were capable of proceeding through the polyol pathway but did not form detectable amounts of glucose-6-phosphate (Fig. 2B). The arrest at [^{13}C]4/6-fluorodeoxysorbitol could be the result of the reduction of aldose reductase activity either through active-site water displacement or through catalytically detrimental interactions with the active-site-adjacent specificity pocket

(29,30). Notably, neither the C_1 - nor the C_6 -fluorinated analog led to trapping, but rather there was a procession through fructolysis to produce fluorolactate. This result was recapitulated *in vivo*, with [^{18}F]6-FDF showing significant bone uptake that was a result of metabolic processing but was not observed using [^{18}F]4-FDF (Fig. 4).

Our metabolic tracing studies suggest that the bone uptake observed with [^{18}F]6-FDF imaging *in vivo* (Fig. 4) may be the result not of tumor cell-induced defluorination but of lactate formation (Fig. 2). Lactate is actively pumped out of tumor cells by influx-efflux monocarboxylate transporters 1 and 4, which contribute to the acidic tumor microenvironment that is a hallmark of solid tumors (31,32). The direct mechanism of radiofluorinated metabolite uptake by bone remains to be uncovered; however, it is known that osteoblasts express monocarboxylate transporter 1 and actively take up lactate (33–35). Additionally, extratumoral metabolism may also contribute to radioactivity uptake in the bone, as hepatic lactate metabolism through lactate dehydrogenase can produce pyruvate with a potential for defluorination (36). By any mechanism, both *in vitro* and *in vivo* data demonstrate that radiodeoxyfluorination of fructose at C_4 , but not at C_6 , can subvert cellular radiometabolite loss and bone accumulation.

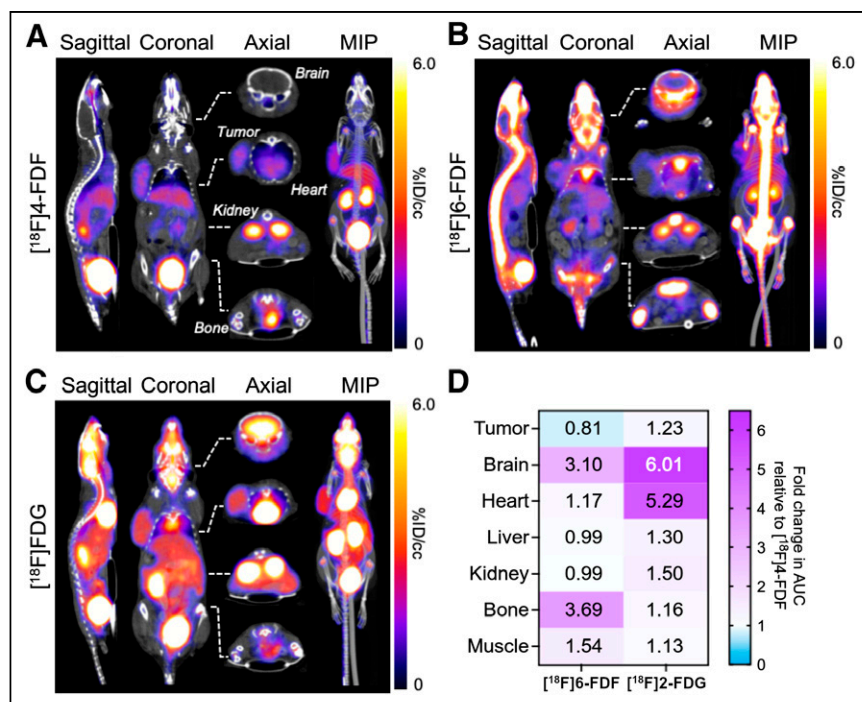


FIGURE 4. Comparative PET/CT imaging in heterotopic HepG2 xenograft mouse model. (A–C) Summed PET/CT images from 20 to 45 min after intravenous injection of [^{18}F]4-FDF (A), [^{18}F]6-FDF (B), or [^{18}F]FDG (C). Sagittal sections, coronal sections, and maximum-intensity projections are shown, in addition to axial sections at level of brain, heart, liver/kidneys, and hips. (D) Fold change in area under curve for entire time-activity curve in Supplemental Figure 2 for [^{18}F]6-FDF and [^{18}F]FDG normalized to values for [^{18}F]4-FDF. Purple represents increase in AUC, and blue represents decrease in area under curve. %ID = percentage injected dose; AUC = area under curve; MIP = maximum-intensity projection.

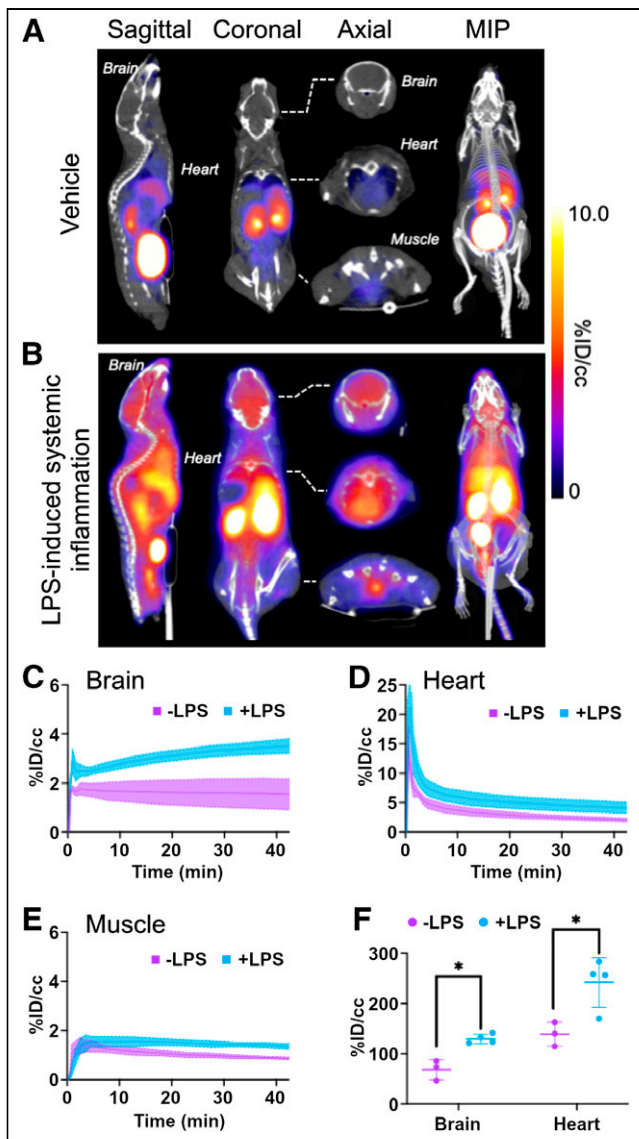


FIGURE 5. Imaging of inflammation in brain and heart. [^{18}F]4-FDF PET/CT was performed on mice receiving vehicle (A) or bacterial cell wall lipopolysaccharide (B) 24h after injection. Sagittal, coronal, maximum-intensity projection, and axial sections of brain, heart, and muscle are shown. (C–E) Time–activity curves for brain (C), heart (D), and muscle (E) for mice receiving vehicle (–LPS, purple) or lipopolysaccharide (+LPS, blue). Solid lines are means, and shaded region are SDs. (F) Comparison of time–activity areas under curve for brain and heart regions of interest for mice receiving vehicle (–LPS, purple) or lipopolysaccharide (+LPS, blue). Plots show individual data points (circles), mean (long line), and SD (vertical line). * $P < 0.05$ by ANOVA followed by Tukey test. %ID = percentage injected dose; LPS = lipopolysaccharide; MIP = maximum-intensity projection.

An important outcome of the stable tracing of fructolysis afforded by [^{18}F]4-FDF was the observation of low uptake in healthy brain and heart (Fig. 5), tissues that are highly glycolytic and associated with high background levels of [^{18}F]FDG uptake (Fig. 4). The low fructolytic background rates in these tissues afforded the sensitive mapping of the neuro- and cardioinflammatory response to systemic lipopolysaccharide administration by [^{18}F]4-FDF (Fig. 5). Therefore, the aldolase-prescribed C_4 radio-deoxyfluorination of fructose resulted in radiotracer trapping on

intracellular uptake and phosphorylation (Fig. 1), overcoming limitations to fructolysis tracing by C_1 and C_6 radioanalogs.

Although [^{18}F]FDG is used clinically to map glucose uptake for diagnostic imaging of traumatic brain injury (37), dementia (38), and Alzheimer disease (39), the estimation of neuroinflammation by [^{18}F]FDG PET is difficult because physiologic glucose uptake may obscure inflammation-specific signal. The presence of inflammatory cells can mask metabolic deficits in neurodegenerative diseases, hindering the use of glucose consumption as a biomarker in these cases (40). Neuronal [^{18}F]FDG uptake in a lipopolysaccharide-treated mouse therefore does not necessarily reflect metabolic state or neuronal damage, as microglial activation and immune cell infiltration confound uptake (41). [^{18}F]FDG PET may also be used for diagnostic imaging of cardiopulmonary inflammation (42), cardiopulmonary infection (43), and atherosclerosis; however, efforts must be made to minimize myocardial glucose metabolism before imaging to reduce the false-positive rate due to the low signal-to-noise ratio (44,45). These efforts rely on a diet-based metabolic switch from glucose to free fatty acids, relying heavily on patient compliance. The low brain and heart uptake in healthy, nonfasting mice described here makes fructose metabolism an attractive biomarker in tissues that are otherwise highly glycolytic and have high [^{18}F]FDG uptake in the absence of disease.

CONCLUSION

The metabolic flux of deoxyfluorofructose was characterized by heavy-isotope labeling. [U^{13}C]–1-FDF exhibited limited polyol metabolism, whereas both [U^{13}C]–6-FDF and [U^{13}C]–4-FDF showed polyol pathway involvement. Only [U^{13}C]–4-FDF metabolism halted at [U^{13}C]–4-fluorodeoxyfructose-1-phosphate, supporting its unique ability to be trapped within cells. [^{18}F]4-FDF was synthesized with good molar activity and radiochemical yield. In a HepG2 xenograft mouse model, [^{18}F]4-FDF exhibited tumor accumulation with minimal bone uptake, whereas [^{18}F]6-FDF displayed substantial bone retention. [^{18}F]4-FDF displayed lower accumulation in normal mouse tissues than did [^{18}F]FDG, notably in the brain and heart. As a result, a significant increase in [^{18}F]4-FDF uptake in cardiac and brain tissues was observed after lipopolysaccharide treatment, highlighting the potential of [^{18}F]4-FDF PET/CT for sensitive mapping of cardio- and neuroinflammation in highly glycolytic tissues. Overall, this research provides critical insights into the metabolic fate of deoxyfluorinated fructose analogs and demonstrates the potential of [^{18}F]4-FDF for mapping disease or injury involving cardio- and neuroinflammation. With the ability to safely and effectively map fructolysis in mice, and low uptake in healthy tissues compared with [^{18}F]FDG, [^{18}F]4-FDF offers a clinically viable tool for diagnostic imaging of tissues with a high baseline glycolytic index. As dosimetry is not expected to be limiting, the clinical translation of this biosimilar radiotracer is feasible.

DISCLOSURE

Funding was received from NSERC (RGPIN-2021-03387, to Adam Shuhendler), the Canada Research Chairs Program (950-230754, to Adam Shuhendler), and the Canadian Cancer Society (grant 707503 to Christina Addison and Adam Shuhendler). Metabolites were analyzed at the University of Ottawa Metabolomics Core Facility. This facility is supported by the Terry Fox Foundation and Ottawa University. No other potential conflict of interest relevant to this article was reported.

KEY POINTS

QUESTION: Can fructose metabolism accurately be mapped by PET?

PERTINENT FINDINGS: By installation of radiofluorine at the C₄ position of fructose, fructose metabolism can be accurately mapped because of intracellular trapping of the phosphorylated metabolite. Fructose use was low in the healthy brain and heart but elevated in disease, providing an opportunity for imaging neuro- and cardioinflammation.

IMPLICATIONS FOR PATIENT CARE: The introduction of [¹⁸F]4-FDF opens new doors for mapping inflammation in cardiac and neural diseases with a biosimilar radiotracer based on a modified dietary sugar.

REFERENCES

- Mirtschink P, Krishnan J, Grimm F, et al. HIF-driven SF3B1 induces KHK-C to enforce fructolysis and heart disease. *Nature*. 2015;522:444–449.
- Mirtschink P, Jang C, Arany Z, Krek W. Fructose metabolism, cardiometabolic risk, and the epidemic of coronary artery disease. *Eur Heart J*. 2018;39:2497–2505.
- Williams AL, Khadka V, Tang M, et al. HIF1 mediates a switch in pyruvate kinase isoforms after myocardial infarction. *Physiol Genomics*. 2018;50:479–494.
- Johnson RJ, Gomez-Pinilla F, Nagel M, et al. Cerebral fructose metabolism as a potential mechanism driving Alzheimer's disease. *Front Aging Neurosci*. 2020;12:560865.
- Spagnuolo MS, Iossa S, Cigliano L. Sweet but bitter: focus on fructose impact on brain function in rodent models. *Nutrients*. 2020;13:1.
- Chen C, Zhang Z, Liu C, et al. ATF4-dependent fructolysis fuels growth of glioblastoma multiforme. *Nat Commun*. 2022;13:6108.
- Liu H, Huang D, McArthur DL, Boros LG, Nissen N, Heaney AP. Fructose induces transketolase flux to promote pancreatic cancer growth. *Cancer Res*. 2010;70:6368–6376.
- Helsley RN, Park SH, Vekaria HJ, et al. Ketoheokinase-C regulates global protein acetylation to decrease carnitine palmitoyltransferase 1a-mediated fatty acid oxidation. *J Hepatol*. 2023;79:25–42.
- Ward PS, Thompson CB. Metabolic reprogramming: a cancer hallmark even Warburg did not anticipate. *Cancer Cell*. 2012;21:297–308.
- Song A, Mao Y, Wei H. GLUT5: structure, functions, diseases and potential applications. *Acta Biochim Biophys Sin (Shanghai)*. 2023;55:1519–1538.
- Hannou SA, Haslam DE, McKeown NM, Herman MA. Fructose metabolism and metabolic disease. *J Clin Invest*. 2018;128:545–555.
- Kolderup A, Svihus B. Fructose metabolism and relation to atherosclerosis, type 2 diabetes, and obesity. *J Nutr Metab*. 2015;2015:823081.
- Hannou JM, Guymer C, Wood JPM, et al. Disturbed glucose and pyruvate metabolism in glaucoma with neuroprotection by pyruvate or rapamycin. *Proc Natl Acad Sci USA*. 2020;117:33619–33627.
- Keshari KR, Wilson DM, Chen AP, et al. Hyperpolarized [2-¹³C]-fructose: a hemiketal DNP substrate for in vivo metabolic imaging. *J Am Chem Soc*. 2009;131:17591–17596.
- Zhang G, Cullen Q, Berishaj M, Deh K, Kim N, Keshari KR. [6,6'-²H₂] fructose as a deuterium metabolic imaging probe in liver cancer. *NMR Biomed*. 2023;36:e4989.
- Haradahira T, Tanaka A, Maeda M, Kanazawa Y, Ichiya YI, Masuda K. Radiosynthesis, rodent biodistribution, and metabolism of 1-deoxy-1-[¹⁸F]fluoro-D-fructose. *Nucl Med Biol*. 1995;22:719–725.
- Wuest M, Trayner BJ, Grant TN, et al. Radiopharmacological evaluation of 6-deoxy-6-[¹⁸F]fluoro-D-fructose as a radiotracer for PET imaging of GLUT5 in breast cancer. *Nucl Med Biol*. 2011;38:461–475.
- Wuest M, Hamann I, Bouvet V, et al. Molecular imaging of GLUT1 and GLUT5 in breast cancer: a multitracer positron emission tomography imaging study in mice. *Mol Pharmacol*. 2018;93:79–89.
- Bouvet V, Jans HS, Wuest M, et al. Automated synthesis and dosimetry of 6-deoxy-6-[¹⁸F]fluoro-D-fructose (6-[¹⁸F]FDF): a radiotracer for imaging of GLUT5 in breast cancer. *Am J Nucl Med Mol Imaging*. 2014;4:248.
- Boyle AJ, Murrell E, Tong J, et al. PET imaging of fructose metabolism in a rodent model of neuroinflammation with 6-[¹⁸F]fluoro-6-deoxy-D-fructose. *Molecules*. 2022;27:8529.
- Fushinobu S, Nishimasu H, Hattori D, Song HJ, Wakagi T. Structural basis for the bifunctionality of fructose-1,6-bisphosphate aldolase/phosphatase. *Nature*. 2011;478:538–541.
- Shrum B, Anantha RV, Xu SX, et al. A robust scoring system to evaluate sepsis severity in an animal model. *BMC Res Notes*. 2014;7:233.
- Tee SS, Kim N, Cullen Q, et al. Ketoheokinase-mediated fructose metabolism is lost in hepatocellular carcinoma and can be leveraged for metabolic imaging. *Sci Adv*. 2022;8:eabm7985.
- Suchý M, Charlton TA, Ben RN, Shuhendler AJ. Synthesis of natural/¹³C-enriched D-tagatose from natural/¹³C-enriched D-fructose. *Carbohydr Res*. 2021;507:108377.
- Luurtsma G, Pichler V, Bongarzone S, et al. EANM guideline for harmonisation on molar activity or specific activity of radiopharmaceuticals: impact on safety and imaging quality. *EJNMMI Radiopharm Chem*. 2021;6:34.
- Yang D, Dai X, Xing Y, et al. Intrinsic cardiac adrenergic cells contribute to LPS-induced myocardial dysfunction. *Commun Biol*. 2022;5:96.
- Batista CRA, Gomes GF, Candelario-Jalil E, Fiebich BL, de Oliveira ACP. Lipopolysaccharide-induced neuroinflammation as a bridge to understand neurodegeneration. *Int J Mol Sci*. 2019;20:2293.
- Pauly TA, Ekstrom JL, Beebe DA, et al. X-ray crystallographic and kinetic studies of human sorbitol dehydrogenase. *Structure*. 2003;11:1071–1085.
- Rechlin C, Scheer F, Terwesten F, et al. Price for opening the transient specificity pocket in human aldose reductase upon ligand binding: structural, thermodynamic, kinetic, and computational analysis. *ACS Chem Biol*. 2017;12:1397–1415.
- Sandner A, Ngo K, Sager CP, et al. Which properties allow ligands to open and bind to the transient binding pocket of human aldose reductase? *Biomolecules*. 2021;11:1837.
- Pérez-Tomás R, Pérez-Guillén I. Lactate in the tumor microenvironment: an essential molecule in cancer progression and treatment. *Cancers (Basel)*. 2020;12:3244.
- Wang Z-H, Peng W-B, Zhang P, Yang X-P, Zhou Q. Lactate in the tumour microenvironment: from immune modulation to therapy. *EBioMedicine*. 2021;73:103627.
- Sasa K, Yoshimura K, Yamada A, et al. Monocarboxylate transporter-1 promotes osteoblast differentiation via suppression of p53, a negative regulator of osteoblast differentiation. *Sci Rep*. 2018;8:10579.
- Luo Y, Gou H, Chen X, Li L, Wang X, Xu Y. Lactate inhibits osteogenic differentiation of human periodontal ligament stem cells via autophagy through the MCT1-mTOR signaling pathway. *Bone*. 2022;162:116444.
- Zhu Z, Chen Y, Zou J, et al. Lactate mediates the bone anabolic effect of high-intensity interval training by inducing osteoblast differentiation. *J Bone Joint Surg Am*. 2023;105:369–379.
- Rabinowitz JD, Enerbäck S. Lactate: the ugly duckling of energy metabolism. *Nat Metab*. 2020;2:566–571.
- Jassam YN, Izzy S, Whalen M, McGavern DB, El Khoury J. Neuroimmunology of traumatic brain injury: time for a paradigm shift. *Neuron*. 2017;95:1246–1265.
- Kato T, Inui Y, Nakamura A, Ito K. Brain fluorodeoxyglucose (FDG) PET in dementia. *Ageing Res Rev*. 2016;30:73–84.
- Marcus C, Mena E, Subramaniam RM. Brain PET in the diagnosis of Alzheimer's disease. *Clin Nucl Med*. 2014;39:e413–e422.
- Backes H, Walberer M, Ladwig A, et al. Glucose consumption of inflammatory cells masks metabolic deficits in the brain. *Neuroimage*. 2016;128:54–62.
- Szöllösi D, Hegedűs N, Veres DS, et al. Evaluation of brain nuclear medicine imaging tracers in a murine model of sepsis-associated encephalopathy. *Mol Imaging Biol*. 2018;20:952–962.
- Bertagna F, Bisleri G, Motta F, et al. Possible role of F18-FDG-PET/CT in the diagnosis of endocarditis: preliminary evidence from a review of the literature. *Int J Cardiovasc Imaging*. 2012;28:1417–1425.
- Eibschutz LS, Rabiee B, Asadollahi S, et al. FDG-PET/CT of COVID-19 and other lung infections. *Semin Nucl Med*. 2022;52:61–70.
- Cussó L, Vaquero JJ, Bacharach S, Desco M. Comparison of methods to reduce myocardial ¹⁸F-FDG uptake in mice: calcium channel blockers versus high-fat diets. *PLoS One*. 2014;9:e107999.
- Wykrzykowska J, Lehman S, Williams G, et al. Imaging of inflamed and vulnerable plaque in coronary arteries with ¹⁸F-FDG PET/CT in patients with suppression of myocardial uptake using a low-carbohydrate, high-fat preparation. *J Nucl Med*. 2009;50:563–568.